Optics and Lasers in Engineering 163 (2023) 107437

Contents lists available at ScienceDirect

Optics and Lasers in Engineering

journal homepage: www.elsevier.com/locate/optlaseng

Axicon lenses with chiral-focusing properties modeling by means of analytical functions

Enrique Moreno [a,*], Jean-Philippe Colombier [b]

[a] Dept. of Electromagnetic Field, Faculty of Electrical Engineering, CTU Technická 2, 166 27 Prague 6 - Dejvice, Czech Republics
[b] Univ Lyon, UJM-St-Etienne, CNRS, IOGS, Laboratoire Hubert Curien UMR 5516, Saint-Etienne F-42023, France

ARTICLE INFO

Keywords:
Micro axicon
Asymmetrical lens
Chirality flux
Nonlinear effects in optics
Electromagnetic patterns on metals
Lens as Maxwell boundary conditions
Symmetric and non-symmetric Bessel beams and simulation of non-linear optics
General vector auxiliary differential equation method
FDTD-DPW

ABSTRACT

Axicon lenses exhibit a large focal depth that generates an energy distribution, resulting in non-diffracting beams' generation. These light structures are called Bessel beams and show numerous important applications in optical signal processing, imaging, transparent material processing, and even in metal drilling/cutting manufacturers. Asymmetrical and twisted axicon-lenses are boundary conditions on the Maxwell equation able to generate complex-structured light fields with specially designed intensity, phase, and polarization distributions. This paper presents a set of analytical functions that allows the definition of such surfaces with absolute freedom in relation to the lens profile. Obviously, before manufacturing any lens, it is necessary to compute its electromagnetic output in order to save resources. In this sense, we have studied some of these lenses by simulation using the well-known finite difference method in the time domain. Some necessary verification related to conservative magnitudes, such as the Poynting vector, have been done analytically and numerically. The numerical results show the distribution of iso-values corresponding to the electric field and 3D-vectorial representation of the chirality flux and the Poynting vector. Finally, by means of discrete fast Fourier transform, it is shown the field distributions as well as the power before and after the lens per frequency.

1. Introduction

The first axicon was proposed in 1954 for astronomical purposes in telescopes that were unconscious of some of its optical properties [1]. Nevertheless, what is indeed an axicon? An axicon is a dielectric cone (a transparent cone to light) capable of focusing parallel incident light on a narrow segment along the optical axis. Compared with a common lens that focuses in the Rayleigh range, the axicon distinguishes itself by its very large depth of focus (DOF), where transverse intensity distribution is almost unchanged along the optical axis. This property is related to one of the universal phenomena of physics well understood, which is diffraction. Since de Broglie's postulate associates particle momentum with the inverse of the wavelength, diffraction is the fundamental basis for quantum-mechanical uncertainty relations introduced by Heisenberg. However, in 1987 Durnin pointed out that the Helmholtz equation has a class of diffraction-free mode solutions [2]. Of course, plane waves are diffraction-free mode solutions of the Helmholtz equation, but Durnin's diffraction-free modes describe well-defined beams with narrow beam radii. Here the central maximum beam is on the order of one wavelength without being subject to diffracted spreading. This theoretical solution was called the Bessel beam, and the first experimental proof was published in the same year [3]. It is essential to point out that any diffraction-free beam must be of infinite cross-section, and the Bessel beam is no exception. In theory, the beam cross-section pattern extension is infinite. However, the intensity gradient from the central maximum is extremely abrupt, considering that the energy is residual beyond a couple of maximums and cannot be measured experimentally. Taking this into consideration, Durnin compared Bessel and Gaussian beams [4] and defined three interesting properties of Bessel beams:

- The transverse intensity distribution is independent of the propagation distance.
- The effective width of the central core of the beam is in the order of one wavelength.
- Bessel beams are easily realizable by using only simple optical elements.

The first time a Bessel beam was generated in a laboratory was by collimated light, which illuminates a circular slit in the focal plane of this lens [3]. It is important to note that the slit is in front of the lens and not behind it. Although a realistic Bessel beam would require an infinite amount of energy to be created, an axicon generates a close approximation with nearly non-diffracting properties within the axicon's depth of focus (DOF). Therefore, the above assertion is true, and Bessel beams are easily realizable using only simple optical elements. Perhaps

* Corresponding author.
E-mail address: enrique@moreno.ws (E. Moreno).

https://doi.org/10.1016/j.optlaseng.2022.107437
Received 8 July 2022; Received in revised form 7 November 2022; Accepted 10 December 2022
Available online 10 January 2023
0143-8166/© 2022 Elsevier Ltd. All rights reserved.

it would have been more interesting to compare the Bessel beam with the Airy beam instead of the Gauss beam. An Airy beam is an invariant propagation wave whose main intensity lobe propagates along a curved parabolic trajectory while being resilient to perturbations (it is self-healing). This beam type can be obtained from a combination of cylindrical lenses [5]. Finally, it is interesting to mention that there are also acoustic Bessel beams [6].

The properties of the particular electromagnetic spatial field distribution, which is generated by an axicon, allow several applications such as plasma and atomic waveguides [7,8], spatial alignment, laser machining, optical coherence tomography, energy concentration, optical readout, and processing [8]. These capabilities are highly demanded in various applications, including optical tweezers [9], laser material processing [10], lithography [11], and even metal drilling due to their potential to make negative electromagnetic pressure while traveling [12]. There are several types of axicons, such as a micro-optical structures on quartz glass plates [13], classical prism [14], light sword optical elements [15], conical light sword optical beams generated by twisted conical geometries [16,17], and others [16,18,19]. In summary, these axicon lenses are defined by means of complicated three-dimensional surface shapes. In this context, the axicons that have a micrometric size are particularly interesting. Thus, we define a lens with "conical geometry" of micrometric size as micro-axicon or μ-axicon. Downscaling the size of bulk optical axicons to micrometer length scale via the development of advanced fabrication techniques significantly expands the application range of classical axicons [17,20–22]. Moreover, microaxicons occupy an important place in micro- and nano-optics applications [8,17,23–29]. We consider that some publications present improvements of the classical conical axicon: gradient index axicon [30], axicon with a spiral-shaped base [31], axicons coupled with either a spiral phase plate [32], or other refractive elements [17], as well as logarithmic [8,17] and fractional axicons [17]. Some authors suggest microaxicons obtained by wrinkling the conical surface of a usual axicon [33]. Such wrinkled axicons, created by cusp deformations (hypocycloidal and epicycloidal) of the circular shape of a conical lens, were fabricated using a rather complicated and time-consuming three-dimensional technique where a direct laser writes via two-photon photopolymerization a liquid resin. This means that by using a femtosecond laser, the nano-fabrication of micro-lenses via two-photon polymerization of resins permits the production of these surface profiles. The current work could be used in this segment as a creative, robust, and fertile source of precise mathematical coordinates for a desirable surface, or it would be better to say a desirable electromagnetic radiation pattern. Furthermore, axicon micro-lenses fabricated with this technique have already demonstrated excellent optical characteristics [8]. The greatest difficulty comes from the need to program the sequence of pulsed laser shots to generate surfaces and ultimately to have an algorithm that defines appropriate surfaces (To know perfectly the coordinates of the axicon surface is essential) in the two-photon polymerization process. In addition, there are other technologies for lens production as direct laser ablation of various targets (such as metals, semiconductors, azopolymers, and even liquid-phase resin [18,34–36]) with specially designed laser beams recently emerged as a promising route towards the direct formation of helical-shaped microstructures [17]. In those cases, analytical knowledge about the lens surface coordinates is an essential step in these techniques. Such microstructures exhibit properties of 3D twisted microaxicons [17]. Therefore, 3D twisted μ-axicons designed by precise mathematical expressions have great utility in electromagnetic nano- and micro-structures, which is the goal of this work. As far as we know, in the literature, few analytical functions allow the topological description of an asymmetric μ-axicon. The novelty of this work lies in offering analytical expressions to topographically model the surfaces of these lenses with a large degree of freedom. Even so, in essence, these mathematical surfaces are nothing more than mathematical boundary conditions for a differential problem of partial differential equations (Maxwell's equations).

Hence in the present manuscript, we provide a way to generate any symmetric or asymmetric axicon lens (either of a rectilinear or twisted profile). In the case of twisted axicons, they are generated by using a multivalued function of several surfaces. Later we study the electromagnetic beams induced by these axicons with the help of a numerical approach to finite differences in the time domain. In order to enrich the content of this manuscript, analytical relationships between conservative quantities, such as the Poynting vector and the chirality flux, have been derived. This task also has the intention to validate the results (To guarantee energy conservation is not enough). It should also be noted that the behavior of the simulated conservative vector magnitudes coincides with the expected one. We can numerically and qualitatively predict those relationships based on the analytical relationships established between the chirality vector and the Poynting vector. We have also used one of our analytical designs to generate a virtual lens and feed a numerical simulator. Therefore, we get, as a result, the redistribution of electromagnetic radiation in a spiral form, presenting different spatial distributions for different frequencies after having passed through the lens. At the same time, it has been verified, through the use of one of the lenses defined here, that these analytic expressions are verified numerically. Note that for non-symmetrical lenses, its optical properties cannot be described or captured by parameters widely used in optics. The very nature of the lens adds information to the pattern of electromagnetic radiation it generated. This information has to be additionally considered in the descriptive way of parameterizing the lens. It is understood that simulation is a natural way to characterize this type of lens. Finally, this manuscript is divided into five sections. In Section 2, we present a set of analytical parametric expressions able to generate complex twisted axicons. In Section 3, we derive the analytical relationships that are established between the conservative magnitudes. In Section 4, some results are explored, and finally, in Section 5, conclusions are summarized.

2. Analytical model of lenses

We define the surface shape revolving around Z-axis a 1D profile given by one analytical example. For instance, we suggest four equations in (1) that lead to the surfaces depicted in Fig. 2a). Of these four profiles, the first corresponds to a symmetrical axicon, and the one with a logarithmic-curved surface provides the desired performance combining both the property of a cone axicon and uniform intensity distribution along the optical axis [8]. On the other hand, these profiles are quite free and admit piecewise functions, discontinuous functions, nonlocal defined derivative functions, and even interpolations in the form of a series of orthonormal functions. Also, parametric equations, such as the harmonic solution, could be employed.

$$f_r(z)=\begin{cases} f_{lin}(z)=\dfrac{R(z_1-z)}{h} & \text{Linear } \mu\text{-axicon lens}\\ f_{exp}(z)=\dfrac{R\left(e^{-b_0(z-z_1)}-1\right)}{e^{b_0 h}-1} & \text{Exponential } \mu\text{-axicon tip lens}\\ f_{log}(z)=\sqrt{\dfrac{1}{b_1}\ln\left(\dfrac{h}{h+(z-z_1)(1-e^{-b_1R^2}}\right)} & \text{Logarithmic } \mu\text{-axicon round lens}\\ f_{cos}(z)=R\cos\left(\dfrac{\pi(z-z_0)}{2h}\right) & \text{Cosine } \mu\text{-axicon lens}\\ c_1 f_{lin}^{b_1}(z)+c_2 f_{exp}^{b_2}(z)+c_3 f_{log}^{b_3}(z)+c_4 f_{cos}^{b_4}(z)+c_5 f_{other}^{b_5}(z) \quad c_i\in\mathbb{R} & \text{Combinations with } b_i=1 \text{ or } b_i\neq 1. \end{cases} \tag{1}$$

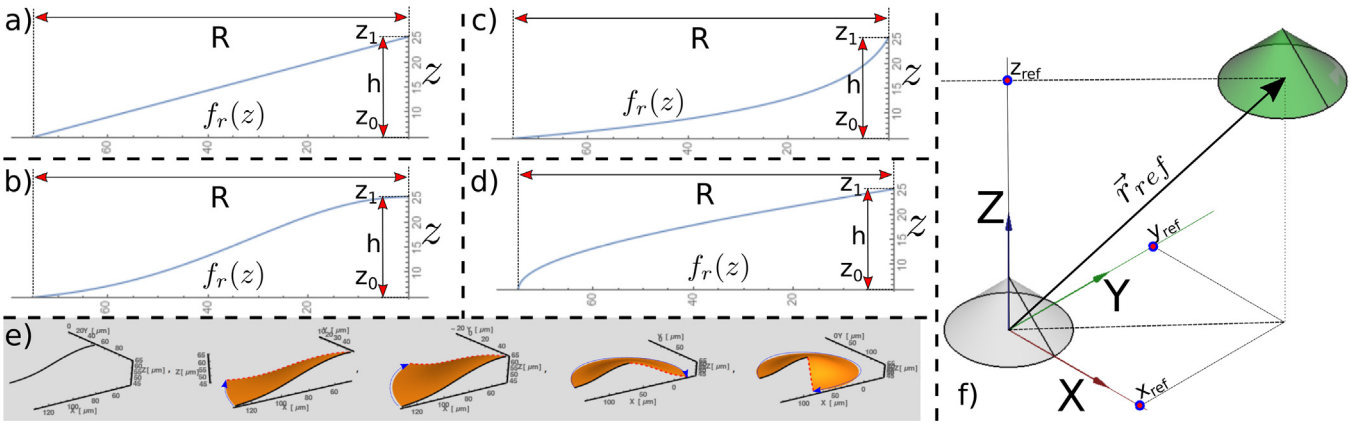


Fig. 1. It is important to note that R=75 μm is the lens radii, z_0=5 μm is the origin of the lens thickness, z_1=5 μm is the end of the lens thickness, z_{ref}=40 μm is the lens position on the Z-axis and h=z_1-z_0=20 μm is the lens thickness. Notwithstanding, z_{ref} is given in the global system of coordinates where the FDTD computational domain is defined. Meanwhile, z_0 and z_1 are at the local system of coordinates where the lens is located. a) Plot of the linear μ-axicon lens profile. b) Plot of the exponential μ-axicon lens profile. c) Plot of the logarithmic μ-axicon lens profile. d) Plot of the cosine μ-axicon lens profile. e) The figure shows the lens construction procedure. The continuous black line is the starting profile that rotates in the dextro-rotatory direction as indicated by the blue arrow and ends in the dashed red line. f) The figure shows the positioning of the lens with respect to the origin, given that the parametric constructions take place at the origin.

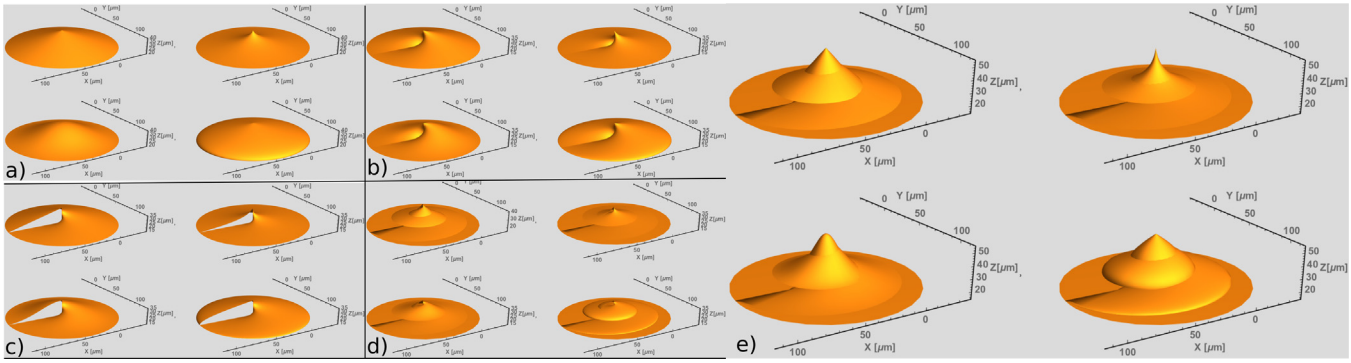


Fig. 2. From top-left to bottom-right linear, exponential, logarithmic and harmonic μ-axicon lenses surfaces. The reader should note that if the details of this figure, such as the labels on the axes or their numerical values, are small, they can always consult the supplementary material where these figures are created and can be viewed in detail [37]. a) Symmetrical lenses. b) Asymmetrical lenses with a continuous profile. c) Asymmetrical lenses with a discontinuous. d) Twisted symmetrical lenses with a discontinuous tip surface. e) Twisted asymmetrical lenses with a continuous tip surface.

In Fig. 1a), we introduce a linear profile, in Fig. 1b) an exponential function, in Fig. 1c) a logarithmic profile, and finally, in Fig. 1d) a profile with a cosine shape. All these profiles or functions are examples of an infinite set of possible functions. In turn, these functions can be combined linearly or not to generate other profiles. The three-dimensional construction of the surfaces is made from a rotation of these profiles, as shown in figure Fig. 1e), in a clockwise direction. Finally, it is necessary to explain that all parametric construction is done around the origin. To displace the surfaces with respect to this point, a displacement vector $\vec{r}_{ref}$, that has three coordinates $(x_{ref}, y_{ref}, z_{ref})$, is necessary. This is what Fig. 1f) illustrates.

In the following subsections, we introduce the different analytical functions and classify them paying attention to their symmetry.

2.1. Symmetrical lenses

The classical micro-axicon lenses are obtained easily using the below parametric expressions (2)–(4):

$$f_x(\theta, z) = f_r(z)\cos(\theta) + x_{ref} \tag{2}$$

$$f_y(\theta, z) = f_r(z)\sin(\theta) + y_{ref} \tag{3}$$

$$f_z(z) = z + z_{ref} \tag{4}$$

Where the angle θ, as shown in Fig. 1e), represents the construction by rotation of the surface through the profile that we have generated by means of the radial function $f_r(z)$ illustrated in figures Fig. 1a–d). We can explain this method. In Fig. 1)e, we can see that starting from a profile in a continuous black line and rotating it through an angle θ in a clockwise direction, as indicated by the blue arrow in the figure, we arrive at the dashed red line. In this process, a surface is generated. This procedure explains how we build each surface. In summary, we rotate the profile given by the $f_r(z)$ function by an angle θ to generate the surface of the lens.

2.2. Asymmetrical lenses

We can replace the last Eq. (4) with the Eq. (7) and find out a single continuous surface when $\eta = \frac{1}{2}$, as Fig. 2b) shows, or an asymmetrical surface with an abrupt, discontinuous step, as Fig. 2c) sketches when $0 < \eta < \frac{1}{2}$.

$$f_x(\theta, z) = f_r(z)\cos(\theta) + x_{ref} \tag{5}$$

$$f_y(\theta, z) = f_r(z)\sin(\theta) + y_{ref} \tag{6}$$

$$f_z(\theta, z) = (z - z_0)\cos(\eta\theta) + z_{ref} \tag{7}$$

Where η is a connection between the evolution in the height of the surface and the angle θ. The lens surface's upper bound is determined by a periodic function, the cosine, according to our definition in the Eq. (7). Here we have chosen the parameter η in a form that the cosine changes so as to guarantee the continuity of the lens surface (that means $\eta = 1/2$). The cosine is a bounded function. Hence, for any other value of η within the specified range, there is an approximation from continuity to the steepest step chosen.

2.3. Twisted asymmetrical lenses

Also, we can define a multivalued function with several surfaces equivalent to a twisted axicon lens. The set of analytical Eqs. (8)–(10) allows a geometry, as shown in Fig. 2d).

$$f_x(\theta, z) = f_r(z)\cos(\theta)e^{-c\theta} + x_{ref} \tag{8}$$

$$f_y(\theta, z) = f_r(z)\sin(\theta)e^{-c\theta} + y_{ref} \tag{9}$$

$$f_z(\theta, z) = \sqrt{\theta} z^{\frac{jump}{2}} + z_{ref} \tag{10}$$

However, the top surfaces portrayed in Fig. 2d) suffer from an abrupt, discontinuous step.

2.4. Twisted symmetrical lenses

Finally, we can close the top surface mentioned in the above subsection replacing the set of parametric functions (8)–(10) with the set (11)–(13):

$$f_x(\theta, z) = \begin{cases} f_r(z)\cos(\theta)e^{-c\theta} + x_{ref} & \theta < \theta_{limit} \\ f_r(z)\cos(\theta)e^{-c\theta_{limit}} + x_{ref} & \theta \geqslant \theta_{limit} \end{cases} \tag{11}$$

$$f_y(\theta, z) = \begin{cases} f_r(z)\sin(\theta)e^{-c\theta} + y_{ref} & \theta < \theta_{limit} \\ f_r(z)\sin(\theta)e^{-c\theta_{limit}} + y_{ref} & \theta \geqslant \theta_{limit} \end{cases} \tag{12}$$

$$f_z(\theta, z) = \begin{cases} \sqrt{\theta} z^{\frac{jump}{2}} + z_{ref} & \theta < \theta_{limit} \\ \sqrt{\theta_{limit}} z^{\frac{jump}{2}} + z_{ref} & \theta \geqslant \theta_{limit} \end{cases} \tag{13}$$

Note that an upper limit to the top lens surface versus the angle θ has been imposed on the function, starting from a certain limit angle. This is done to obtain a symmetrical upper surface. That is, we finish one of the essential elements of an axicon lens, the vertex/tip, on a symmetrical surface. The result of these functional constructions can be visualized in the figures that appear below. In Fig. 2a), we can see the representation of the surfaces generated by the set of Eqs. (2)–(4). Fig. 2b depicts the surfaces generated by the set of Eqs. (5)–(7) (with $\eta = 1/2$). Figure 2c) portrays the surfaces generated by the set of Eqs. (5)–(7) (with $\eta < 1/2$). Figure 2d shows the surfaces generated by the set of Eqs. (8)–(10). Finally, Fig. 2e illustrates the surfaces generated by the set of Eqs. (11)–(13).

When we have mathematically generated surfaces, there is a multivalued dependency between the pair of coordinates of the XY-plane and the elevation of the surface corresponding to the surfaces. Thus, if we have to export the point cloud corresponding to the external surface that encloses the lens, we have to do it by taking the appropriate surface. If we take any of the three surfaces, there is not possible to reconstruct the lens. Multivalued means that we have three different heights for any point of the XY-plane. Obviously, we are not always on the higher surface. We are indeed trying to build the outer topological frontier of the lens, but in each region of the XY-plane we have to take the corresponding surface. This is indicated in Fig. 3, there is a division of the XY-plane by regions and in each region, we take a surface for the lens construction.

The axicon lens characterization is always possible. Although we have a continuous variation of the slope, that is, in Fig. 4 the angle $\alpha(z)$ changes its value with the radial position (in our case z), it is always possible to find a maximum value for this angle. From there, it is possible to carry out a characterization where we define lens parameters. The problem comes when we try to characterize, with optical parameters typical of symmetrical lenses, lenses that are asymmetrical. We cannot do that because there is more information in an asymmetric lens. We would have to either define more parameters or make intermediate average values of the classics. In Fig. 4, we can visualize this clearly. Figure 4 shows several cut longitudinal cross-sections of an asymmetric axicon lens. In the figure, the refraction surface profiles for the axicon lens cuts/sections are different. We choose one of them and make the simplification of assuming that α angles are constant in a piecewise form. We can make some definitions for that cutting plane (right side in Fig. 4). Still, it makes little sense when we have other cutting planes with different properties and, therefore, with other optical characterization parameters. In this way, parameters as important as DOF cannot possibly always be defined on the optical axis of the system. Therefore, we can define in the particular longitudinal cross-section plotted in Fig. 4 some parameters as,

$$DOF' = \frac{2R\csc(2\alpha_6)}{\left(\frac{n\cos(\alpha_6)}{\sqrt{1-n^2\sin^2(\alpha_6)}} - 1\right)}\,;\; d_r = L\sum_i^{\alpha_1,\alpha_4}\left[\frac{\frac{n\cos(\alpha_i)}{\sqrt{1-n^2\sin^2(\alpha_i)}} - 1}{\frac{n\sin(\alpha_i)}{\sqrt{1-n^2\sin^2(\alpha_i)}} + \cot(\alpha_i)}\right];$$

$$t_2 \simeq \frac{R\sec^2\left(\frac{\alpha_4+\alpha_6}{2}\right)}{\frac{n(\cos(\alpha_4+\alpha_6)-1)\sec\left(\frac{\alpha_4+\alpha_6}{2}\right)}{\sqrt{2(2+n^2(\cos(\alpha_4+\alpha_6)-1))}} + 1}.$$

Finally, a comment on the simplest determination can be made of these parameters is by numerical derivation of the projections of Maxwell's solutions obtained numerically. Although, it has to be understood that we are not talking about fixed values or scalars but angular functions in many cases.

With the aim to facilitate the usage of the introduced functions, we provide auxiliary or supplementary material that will help the reader in the usage of these functions [37].

In the next section, we employ one of these lenses so as to generate a particular twisted and pulsed Besilian Beam.

3. A link between the chirality flux and the Poynting vector

This section is more related to the results than to the procedure to obtain them. When we speak of results, we are referring to the electromagnetic fields that we obtain after passing a particular distribution of electromagnetic fields through one of the lenses that we have modeled mathematically. The reason for placing this theoretical preamble before the results is to understand the results to some extent. In 1964 a new conservative relationship appeared in [38]. It relates the density of chirality flux to the density of chirality. But what mean these magnitudes? Chirality, or handedness, means that an object or molecule cannot be superimposed on its mirror image by any translations or rotations [39]. Although chirality itself is a qualitative property, chiroptical systems can be quantitatively modeled by chiroptical parameters. Light cannot be chiral in the conventional sense, as it possesses no geometry, but the chirality of light can be defined with certain parameters. Chiral properties arise from the rotating electric and magnetic vector fields as the wave propagates. Light can also carry orbital angular momentum, which creates a helical geometry on the wavefront. The amount of chirality that light carries can be expressed in terms of chiroptical parameters such as the spin-density fluxes, optical helicity fluxes, and orbital and spin angular momenta [40]. Here we consider optical helicity fluxes, in particular the density of chirality flux and the density of chirality. We take expressions (14)–(16) from the bibliographical reference [40], which corresponds to (4)–(6) in the mentioned source. In this form, we

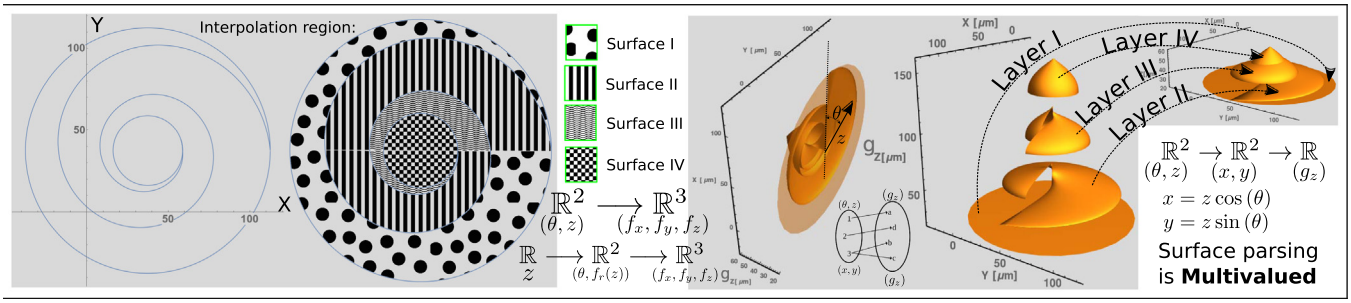


Fig. 3. The figure identifies the lens regions corresponding with the different exported surfaces. The figure also shows the exporting points since the transformation is multivalued. That is why we must be selective with the surface we are considering.

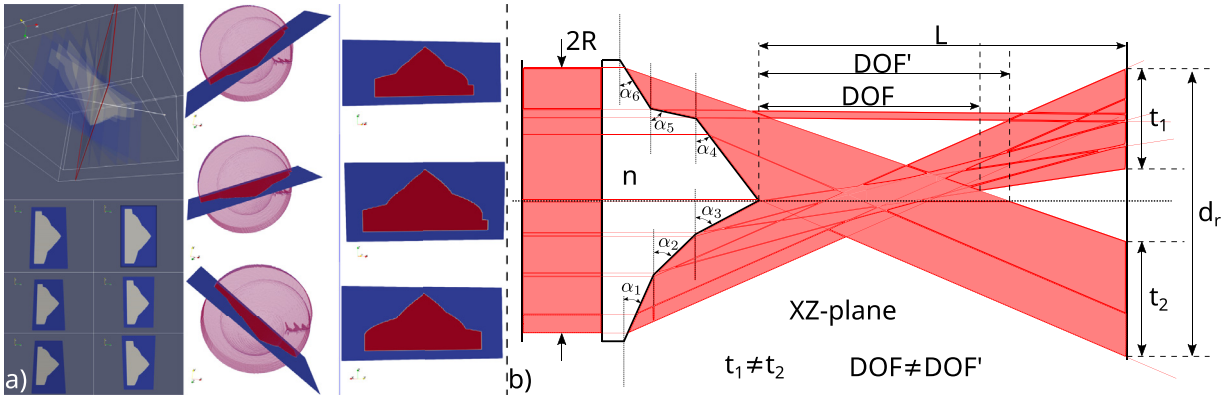


Fig. 4. a) With the help of Paraview, an isometry of the dielectric media present in the simulation has been illustrated using the lens cut by different longitudinal cross-sections. All these sections pass through the system's optical axis, that is, through the vertex of the axicon. We can see a continuous variation of the slope of the angles α, concerning the transverse plane, along the radial direction for each longitudinal section. b) This figure shows a simplified approximation. It illustrates an asymmetric shape for the lens longitudinal cross-section, which would differ for each election of those longitudinal cross-sections. Therefore, the optical parameters are different from the usual ones and simultaneously different for each longitudinal cross-section we consider.

have the following expressions:

$$\nabla\cdot\vec{\Phi}_\chi(\vec{r},t)+\partial_t\chi(\vec{r},t)=-\Big(\vec{J}(\vec{r},t)\cdot\nabla\wedge\vec{E}(\vec{r},t)+\vec{E}(\vec{r},t)\cdot\nabla\wedge\vec{J}(\vec{r},t)\Big)/2 \tag{14}$$

$$\chi(\vec{r},t)=\Big(\epsilon_0\vec{E}(\vec{r},t)\cdot\nabla\wedge\vec{E}(\vec{r},t)+\mu_0\vec{H}(\vec{r},t)\cdot\nabla\wedge\vec{H}(\vec{r},t)\Big)/2 \tag{15}$$

$$\vec{\Phi}_\chi(\vec{r},t)=\Big(\vec{E}(\vec{r},t)\wedge\Big(\nabla\wedge\vec{H}(\vec{r},t)\Big)-\vec{H}(\vec{r},t)\wedge\Big(\nabla\wedge\vec{E}(\vec{r},t)\Big)\Big)/2 \tag{16}$$

Where $\vec{\Phi}_\chi(\vec{r},t)$ is the flux of chirality, $\chi(\vec{r},t)$ the chirality density, $\vec{J}(\vec{r},t)$ the electric current density, $\vec{E}(\vec{r},t)$ the electric field vector, $\vec{H}(\vec{r},t)$ the magnetic field vector, ϵ_0 the electric permittivity of the medium and μ_0 the magnetic permeability of the medium.

In what follows, we will establish a relationship between the Poynting vector and the chirality flux. To this end we will use the Jacobian matrix, where for instance $\nabla\vec{H}(\vec{r},t)=\left(\frac{\partial H_i(\vec{r},t)}{\partial x_j}\right)_{ij}$, so as to define the chirality flux as follows, $\vec{\Phi}_\chi(\vec{r},t)=\Big((\nabla\vec{H}(\vec{r},t))\cdot\vec{E}(\vec{r},t)-\Big(\vec{E}(\vec{r},t)\cdot\nabla\Big)\vec{H}(\vec{r},t)+\Big(\vec{H}(\vec{r},t)\cdot\nabla\Big)\vec{E}(\vec{r},t)-(\nabla\vec{E}(\vec{r},t))\cdot\vec{H}(\vec{r},t)\Big)/2$ and combines it with the curl of the Pointing vector $\nabla\wedge\vec{S}(\vec{r},t)$. Also, we can write the last magnitude using some mathematical identities that permits its combination with the development chirality flux already written, $\nabla\wedge\Big(\vec{E}(\vec{r},t)\wedge\vec{H}(\vec{r},t)\Big)=\Big(\nabla\cdot\vec{H}(\vec{r},t)\Big)\vec{E}(\vec{r},t)-\Big(\nabla\cdot\vec{E}(\vec{r},t)\Big)\vec{H}(\vec{r},t)+\Big(\vec{H}(\vec{r},t)\cdot\nabla\Big)\vec{E}(\vec{r},t)-\Big(\vec{E}(\vec{r},t)\cdot\nabla\Big)\vec{H}(\vec{r},t)$. In this way, after some mathematical operations in which we have used identities, we find a relationship between the chirality flux and the Poynting vector:

$$\vec{\Phi}_\chi(\vec{r},t)=\Big(\nabla\wedge\vec{S}(\vec{r},t)-\Big(\Big(\vec{E}\wedge\nabla\Big)\wedge\vec{H}(\vec{r},t)+\Big(\vec{H}\wedge\nabla\Big)\wedge\vec{E}(\vec{r},t)\Big)\Big)/2 \tag{17}$$

Undoubtedly, the reason why the relationship between conservative magnitudes is important is to demonstrate that one does not derive from the other without another magnitude. Since then, we have been talking about the same magnitude. There would not be two magnitudes but one. Another reason why the relationship between the Poynting vector and chirality flux is important is the possibility of verifying or validating a numerical implementation. If we compute the chirality flux and the Poynting vector numerically, we can check that the relationship holds. Otherwise, our implementation or numerical calculation would be wrong.

It is now interesting to consider a particular case in which the chirality flux can be defined as a partial vector source of the Poynting vector. Therefore, we consider a region of space free of sources or, more specifically, of electrical current densities, where being sufficiently far from the source (electromagnetic field origin), we can assume that we have a far-field zone. We are hence assuming that the chirality density can be related to the chirality flux by the expression,

$$\frac{\partial}{\partial t}\left(\vec{E}(\vec{r},t)\cdot\frac{\partial\vec{H}(\vec{r},t)}{\partial t}+\vec{H}(\vec{r},t)\cdot\frac{\partial\vec{E}(\vec{r},t)}{\partial t}\right)$$
$$=c^2\nabla\cdot\Big(\Big(\vec{E}\wedge\nabla\Big)\wedge\vec{H}(\vec{r},t)+\Big(\vec{H}\wedge\nabla\Big)\wedge\vec{E}(\vec{r},t)\Big) \tag{18}$$

Assuming that the electric field is perpendicular to the magnetic field, we can consider that the divergence term in the equation above is zero (The left hand-side in the above equation is zero when $\vec{E}(\vec{r},t)\perp\vec{H}(\vec{r},t)$).

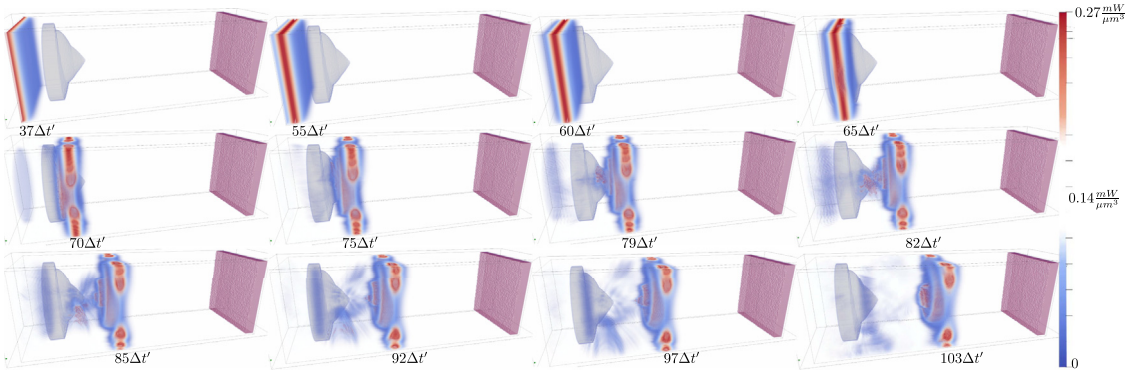


Fig. 5. From left to right and from top to bottom, the figure illustrates the time evolution of the chirality flux module for a pulsed laser beam. What we see is the restructuring process of the electric field module when it interacts with the dielectric lens that we have formed from the cosine function. Each frame appears at the instant of time in which it has been captured. Note that $\Delta t' = 40\Delta_t$ and $\Delta_t = 2.65765 \times 10^{-16} s$.

Therefore, there is a potential vector $\vec{\Omega}(\vec{r},t)$ that leads us to:

$$\nabla \wedge \vec{\Omega}(\vec{r},t) = \left(\vec{E} \wedge \nabla\right) \wedge \vec{H}(\vec{r},t) + \left(\vec{H} \wedge \nabla\right) \wedge \vec{E}(\vec{r},t) \tag{19}$$

In these circumstances, the chirality flux can be determined by curling two vectors, on the one hand the Poynting vector and on the other the potential vector that we have just derived, so $\vec{\Phi}_{\chi}(\vec{r},t) = \frac{1}{2}\nabla \wedge \left(\vec{S}(\vec{r},t) - \vec{\Omega}(\vec{r},t)\right)$. It is in this way that, taken into consideration Helmholtz's theorem, we can assume that the Poynting vector is a partial vector source of the chirality flux. Last but not least, under the conditions that we are assuming of a source-free far-field region, we have a potential vector such that the chirality flux can be obtained from it.

So far, we have presented a mathematical description devoid of physical interpretation, and in consequence, we continue to introduce a physical interpretation. While the Poynting vector is a measure of the electromagnetic power flux through the surface surrounding a region of space, the chirality flux is the local power density that could be found inside that region and whose vector representation is associated with the variation or propagation of the mentioned power density within that region. Likewise, the chirality flux density is the local spatial variation between points of the electromagnetic power density inside the cited region.

4. Results

The configuration of the optical system or computational domain is the one that follows. A pulsed plane wave of wavelength (800 ± 11) nm and a time full width at half maximum of $\sigma_t = 40$fs passes through an axicon lens (with refractive index equal to 1.5) of 100 μm in diameter located 250 μm from a square sheet of metal whose diagonal is $100\sqrt{2}$ μm and its thickness 35 μm. The mathematical models and parameters used in the description, both for the laser and for the numerical method itself, can be found in the bibliographical reference [41]. The numerical engine in [41] is an evolution of a primitive finite difference code in the time domain [42], which is based on other codes [43,44]. This original code has undergone many improvements over time [45–49].

The complexity presented by the analysis of the results gives for a job by itself. However, with the sole purpose of showing the configurations obtainable from mathematically modeled lenses, this section is developed. In this section, we plot some results with the aim of describing the electromagnetic field structure induced by the analytical functions presented in the current work. In [41], we have presented a simulator based on the general vector auxiliary differential equation finite difference time domain technique, which is able to deal with nonlinear effects, such as Kerr and Raman effects and others related to the free charge photoinduced (photoionization, avalanche events, and so on), employing an explicit formulation. The parameters related to the simulations carried out here, as well as the dielectric properties of the media and some other optical details of interest, can be consulted in the bibliographical reference [41]. Therefore, the simulations carried out here share all the technical details regarding the numerical method with the simulator presented in [41].

In Fig. 2e, in the bottom-left corner, appears the continuous cosine axicon, which has been considered in the simulation carried out. We have fed/illuminated the system by an incident light circularly polarized. Fig. 5 illustrates the time evolution for the module of the chirality flux, Eq. (16), for an incident pulsed plane wave circularly polarized.

We can see a spiral distribution of intensity rotating the Z-axis while the Bessel beam propagates in the increasing direction of the Z-axis. If we study the dynamics of the electric field vector along the propagation, we see that its end describes a very similar behavior to an azimuthal trajectory too. This can be clearly seen if we consider different temporal states in the beam propagation and study the vector shape of the electromagnetic field. In Fig. 2e, in the lower right corner, we can see the surface of an axicon lens that, from now on, we call continuous vertex cosine profile axicon lens (CVCPAL). Fig. 6 displays some frames from the simulation that correspond to the Bessel beam vector field formed by a fused-silica CVCPAL. What we see is the time evolution of the Poynting vector after passing through the lens and the flux of chirality at the same time instants. It is evident that the vector field reveals the evolution of the intensity of the pulse locally through the size of the field vectors. In Fig. 6, we can also verify the spiral field distribution produced by the twisted axicon with the harmonic profile. In the figure, the field distribution is not perceived in detail and neither does a color gradient appear to indicate the variations of the magnitudes represented. In [50], there is a set of high-resolution videos where the color gradient that indicates the numerical variation of the magnitudes has not been omitted. At the same time, a certain continuity in its evolution can be seen.

Finally, and in order to quantitatively describe the phenomenology of interaction between the pulsed beam and a metal sheet, we have represented the chirality flux throughout its interaction (in time) with a nickel surface that is not polished and therefore presents a certain roughness. One of the things that we can observe in this interaction is that the energy will not be conserved since the metal acts as a dispersive medium, but there is conservation in the rotating or vortex nature of the light structure. That is, there is reflective conservation as to the vortex structure in the light that emerges after interacting with the metal sheet. Consequently, in Fig. 7, we visualize the temporal evolution of the pulse. For this, a longitudinal cross-section/cut of the computational domain has been made through its diagonal (left part of the figure). In the area where the interaction takes place, we can see how the pulsed laser hits the metal surface and is reflected. To the right of each representation, we can see the evolution, in magnitude and structure, of two vector fields. Fig. 7a shows the flow of chirality, and Fig. 7b plots the electric field.

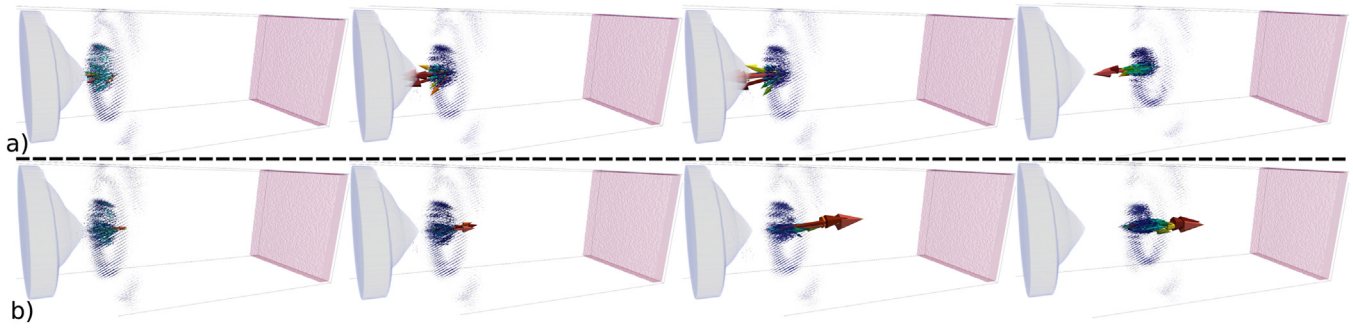


Fig. 6. From left to right, this figure shows the evolution of the vector field corresponding to a) the chirality flux and b) the Poynting vector. What we are seeing is the modification of the corresponding vector field after the passage of a circularly polarized plane wave through the cosine dielectric lens. In these figures, for a matter of increasing space and visualization, the color gradient bars that inform about the values of the magnitudes have been eliminated. This information appears in the high-resolution dynamic animations corresponding to the simulations in [50].

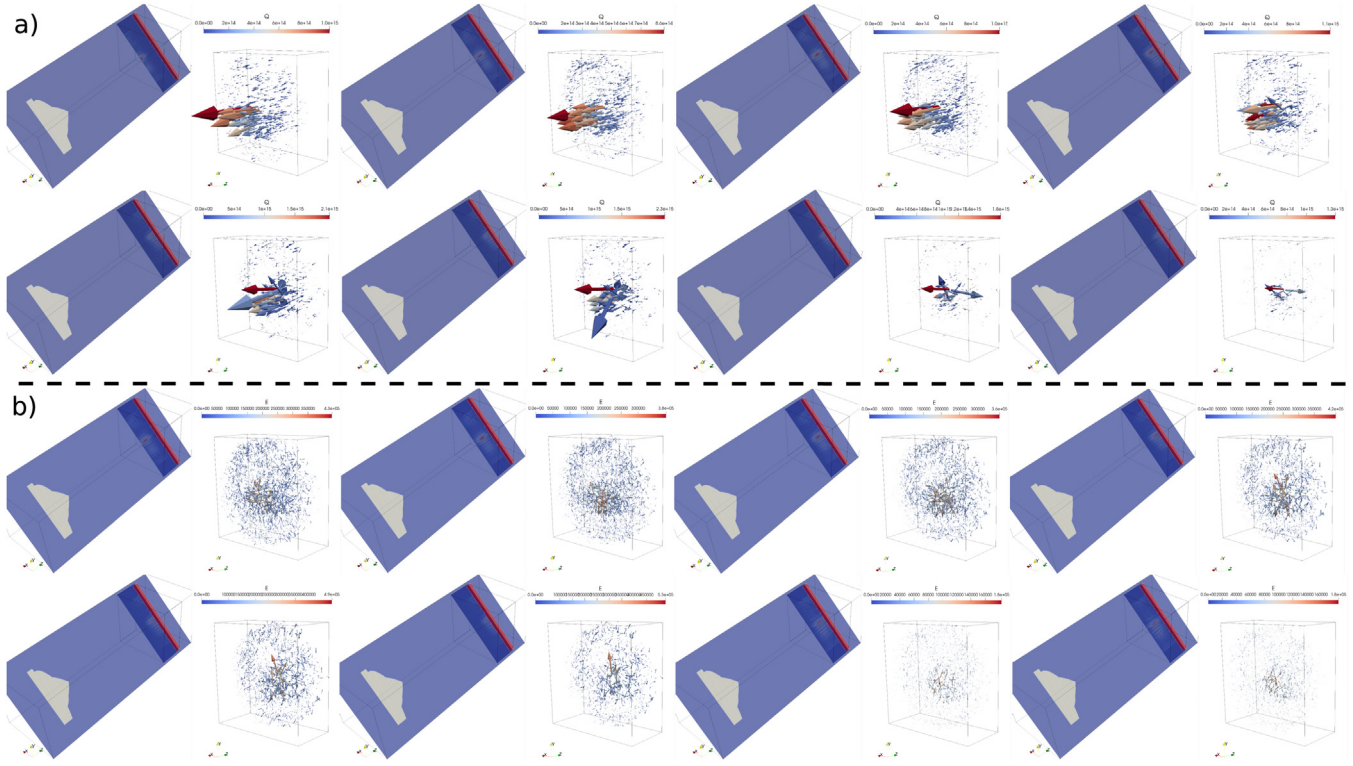


Fig. 7. From top to bottom and from left to right, the figure represents the temporal evolution of a) the chirality flux and b) the electric field. Both magnitudes interact with a metallic surface of a certain roughness. Due to the electromagnetic properties displayed by the metal (we are considering nickel), a strong absorption effect appears. The reader should note that if the details of this figure, such as the labels on the axes or their numerical values, are small, they can always watch a high-resolution animation in [50].

Since it is a pulsed signal, it has a space-time location. We can understand that at a given instant of time t_{place} the pulsed signal is in a region of the computational domain. The entire spatial region occupied by the pulse can be described in terms of time as $t_{place} \pm 5\sigma_t$. Now let us imagine that we want to determine the frequency components that are present in that pulsed electromagnetic structure. To do so, we have to perform the Fourier transform around the instant of time in which the pulse is located at the region of interest. We take as an example of representation the electric field $\vec{E}(\vec{r},t)$. In consequence, we perform the integral with at least five sigmas around that time value, that is,

$$\vec{E}(\vec{r},\omega) = \sqrt{\frac{\beta}{2\pi}} \int_{t_{place}-5\sigma_t}^{t_{place}+5\sigma_t} \vec{E}(\vec{r},t) e^{-j\beta\omega t} dt$$

If we focus only on the lens, without considering the metal sheet, since it is a lossless dielectric and therefore a non-dispersive medium, the uncertainty associated with the wavelength of the laser (which was 11 nm), is the one that gives us the range of frequencies that we must consider $[\nu_{\min}, \nu_{\max}] \equiv \left[\frac{c_0}{\lambda_l+11\ \text{nm}}, \frac{c_0}{\lambda_l-11\ \text{nm}}\right]$ (with $\lambda_l = 800$ nm). Thus, if we place ourselves at an intermediate frequency 375 THz and plot the structure of the electric field in an iso-value representation or directly in a vector field, we get the result shown in Fig. 8. The figure shows the spatial distribution of $\vec{E}(\vec{r},\omega)$ corresponding to the instant in which the pulse has left the lens. This representation of the electric field corresponds to a single frequency that is right in the middle of the interval of frequencies indicated previously. Curiously for different frequencies of the interval $[370, 380]$ THz we have different field distributions. It is extremely difficult to get a vision of the dynamics of the electromagnetic magnitudes presented here through the fixed figures. Therefore, with the sole purpose of facilitating the understanding of the interaction between the lens

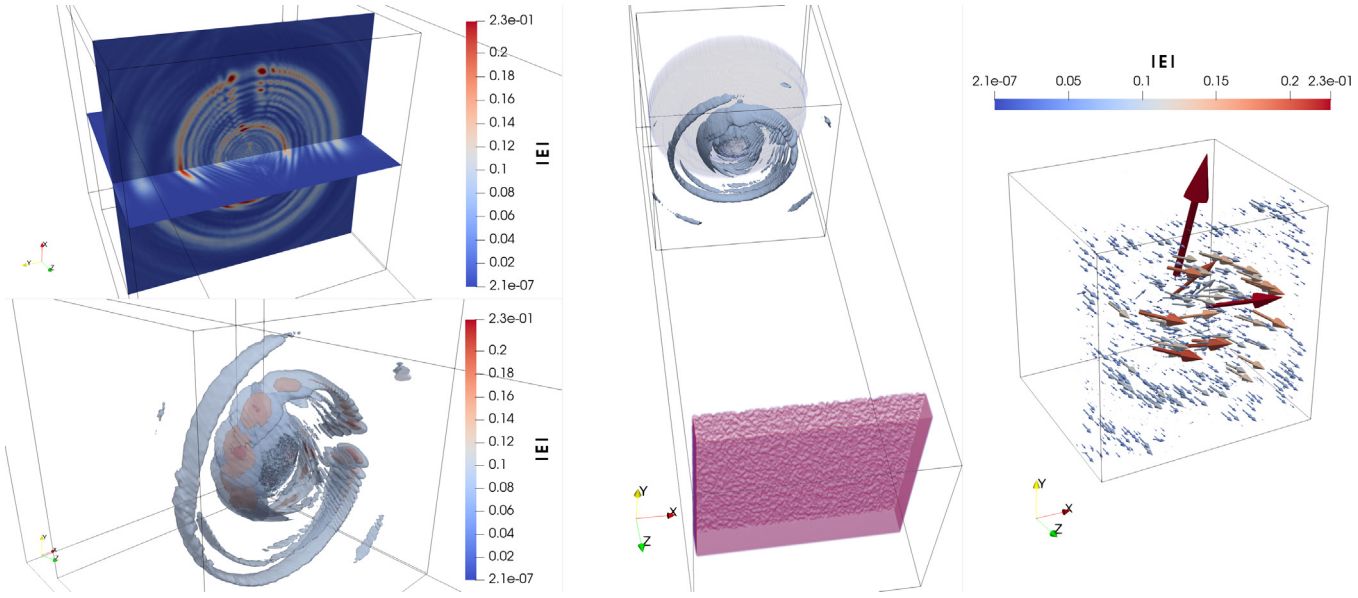


Fig. 8. The figure shows the electric field distribution of the pulsed beam just after the lens for a frequency of $3.75 \cdot 10^{14}$Hz (or a wavelength of 799.447 nm).

and the electromagnetic field, a sequence of videos can be viewed at the YouTube link [50].

Note that to understand what the input to the lens is (type of light), the following notation is used relative to the name of the video AA_BB_CC.

- AA should be replaced by the acronyms LP or CP, which in turn represent linearly polarized light and circularly polarized light, respectively.
- BB should be replaced by the acronyms AL or SL, representing asymmetric and symmetric lenses, respectively.
- CC should be replaced by the acronyms RS or FS, which stands for rough surface and flat surface, respectively.

Although in this manuscript, we are focusing on the mathematical modeling of lenses, it is also important to consider the effect that the pulsed beam has on an objective metal plate. With this idea in mind and thinking about future works, the last element has been added, in which it is assumed that the impact surface can be polished/flat, or rough.

5. Conclusion

The current work explains how, by a simple one-dimensional function, we can construct the surface shape of a lens. In short, we are generating a mathematical boundary condition for Maxwell's equations, which results in an electromagnetic field with the presence of a high asymmetry in its radiative pattern.

We present a set of analytical functions and explain how to build axicon lenses from them. The main idea is that before manufacturing one of these lenses, we can introduce them in a simulator and study the generated beams. At the same time, we will have the topological structure and the coordinates that allow us to print this type of dielectric lens in photo-resin. In the current work, we have confirmed, utilizing simulations carried out through a general vector auxiliary differential equation FDTD method, the exotic polarization structures that can interact with the matter after the lens. Therefore, the method allows the fabrication of lenses able to provide electromagnetic structures with a wide variety of applications. One additional application for the mathematical models presented here would be the study of vorticity conservation properties of light in Bessel beams. In future works, we intend to use this work to carry out studies on these properties of pulsed Bessel beams and their interaction with metals.

Declaration of Competing Interest

The authors declare the following financial interests/personal relationships which may be considered as potential competing interests: Enrique Moreno reports was provided by Czech Technical University in Prague

CRediT authorship contribution statement

Enrique Moreno: Conceptualization, Data curation, Formal analysis, Funding acquisition, Investigation, Methodology, Project administration, Resources, Software, Supervision, Validation, Visualization, Writing – original draft, Writing – review & editing. **Jean-Philippe Colombier:** Conceptualization, Funding acquisition, Methodology, Project administration, Writing – review & editing.

Data availability

No data was used for the research described in the article.

Acknowledgment

The first author would like to thank the CTU Global Postdoc Fellowship Program and its funds that have made this work possible. Also, this work was supported by the LABEX MANUTECH-SISE (ANR-10-LABX-0075) of Université de Lyon, within the Plan France 2030 operated by the French National Research Agency (ANR).

Moreover, the first author would like to thank Pedro González Rodelas from the University of Granada for his kind support with the sampling and extraction clouds of points from the analytical surfaces. Finally, the we wants to thank Lukas Jelinek from CTU in Prague for the suggestions given in the initial draft.

References

[1] McLeod JH. The axicon: a new type of optical element. J Opt Soc Am 1954;44(8):592–7.
[2] Durnin J. Exact solutions for nondiffracting beams. I. The scalar theory. J Opt Soc Am A 1987;4(4):651–4.
[3] Durnin J, Miceli JJ, Eberly JH. Diffraction-free beams. Phys Rev Lett 1987;58:1499–501.
[4] Durnin J, Miceli JJ, Eberly JH. Comparison of bessel and gaussian beams. Opt Lett 1988;13(2):79–80.

[5] Yalizay B, Soylu B, Akturk S. Optical element for generation of accelerating airy beams. J Opt Soc Am A 2010;27(10):2344–6.
[6] Jiménez N, Picó R, Sánchez-Morcillo V, Romero-García V, García-Raffi LM, Staliunas K. Formation of high-order acoustic bessel beams by spiral diffraction gratings. Phys Rev E 2016;94:053004.
[7] Florjaczyk M, Tremblay R. Guiding of atoms in a travelling-wave laser trap formed by the axicon. Opt Commun 1989;73(6):448–50.
[8] Lin X-F, Chen Q-D, Niu L-G, Jiang T, Wang W-Q, Sun H-B. Mask-free production of integratable monolithic micro logarithmic axicon lenses. J Lightwave Technol 2010;28(8):1256–60.
[9] Cabrini S, Liberale C, Cojoc D, Carpentiero A, Prasciolu M, Mora S, et al. Axicon lens on optical fiber forming optical tweezers, made by focused ion beam milling. Microelectron Eng 2006;83(4):804–7. Micro- and Nano-Engineering MNE 2005
[10] Nguyen HD, Moreno E, Rudenko A, Faure N, Sedao X, Mauclair C, et al. Super-efficient drilling of metals with ultrafast non diffractive laser beams. Sci Rep 2022.
[11] Khonina SN, Kazanskiy NL, Khorin PA, Butt MA. Modern types of axicons: new functions and applications. sensors (basel). Sensors MDPI 2021.
[12] Nguyen HD, Sedao X, Mauclair C, Bidron G, Faure N, Moreno E, Colombier J-P, Stoian R. Non-diffractive bessel beams for ultrafast laser scanning platform and proof-of-concept side-wall polishing of additively manufactured parts. Micromachines MDPI 2020.
[13] Kopitkovas G, Lippert T, David C, Wokaun A, Gobrecht J. Fabrication of micro-optical elements in quartz by laser induced backside wet etching. Microelectron Eng 2003;67–68:438–44. Proceedings of the 28th International Conference on Micro- and Nano-Engineering
[14] Kurt H, Turduev M. Generation of a two-dimensional limited-diffraction beam with self-healing ability by annular-type photonic crystals. J Opt Soc Am B 2012;29(6):1245–56.
[15] Kołodziejczyk A, Bar S, Jaroszewicz Z, Sypek M. The light sword optical element–a new diffraction structure with extended depth of focus. J Mod Opt 1990;37(8):1283–6.
[16] Singh BK, Mehta DS, Senthilkumaran P. Conical light sword optical beam and its healing property. Opt Lett 2014;39(7):2064–7.
[17] Khonina SN, Krasnov SV, Ustinov AV, S A Degtyarev A, Porfirev P, Kuchmizhak A, et al. Refractive twisted microaxicons. Opt Lett 2020;45(6):1334.
[18] Toyoda K, Takahashi F, Takizawa S, Tokizane Y, Miyamoto K, Morita R, Omatsu T. Transfer of light helicity to nanostructures. Phys Rev Lett 2013;110:143603.
[19] Sabatyan A, Rafighdoost J. Grating- and checkerboard-based zone plates as an optical array generator with a favorable beam shape. Appl Opt 2017;56(19):5355–9.
[20] Cheong WC, Ahluwalia BPS, Yuan X-C, Zhang L-S, Wang H, Niu HB, et al. Fabrication of efficient microaxicon by direct electron-beam lithography for long nondiffracting distance of bessel beams for optical manipulation. Appl Phys Lett 2005;87(2):024104.
[21] Grosjean T, Saleh SS, Suarez MA, Ibrahim IA, Piquerey V, Charraut D, Sandoz P. Fiber microaxicons fabricated by a polishing technique for the generation of bessel-like beams. Appl Opt 2007;46(33):8061–7.
[22] Kuchmizhak A, Gurbatov S, Nepomniaschii A, Vitrik O, Kulchin Y. High-quality fiber microaxicons fabricated by a modified chemical etching method for laser focusing and generation of bessel-like beams. Appl Opt 2014;53(5):937–43.
[23] Babadjanyan AJ, Margaryan NL, Nerkararyan KV. Superfocusing of surface polaritons in the conical structure. J Appl Phys 2000;87(8):3785–8.
[24] Yu Y-J, Noh H, Hong M-H, Noh H-R, Arakawa Y, Jhe W. Focusing characteristics of optical fiber axicon microlens for near-field spectroscopy: dependence of tip apex angle. Opt Commun 2006;267(1):264–70.
[25] Golub I. Solid immersion axicon: maximizing nondiffracting or bessel beam resolution. Opt Lett 2007;32(15):2161–3.
[26] Goncharenko A, Chang H-C, Wang J-K. Electric near-field enhancing properties of a finite-size metal conical nano-tip. Ultramicroscopy 2007;107(2):151–7.
[27] Wang Y, Yan S, Friberg AT, Kuebel D, Visser TD. Electromagnetic diffraction theory of refractive axicon lenses. J Opt Soc Am A 2017;34(7):1201–11.
[28] Khonina S, Degtyarev S, Savelyev D, Ustinov A. Focused, evanescent, hollow, and collimated beams formed by microaxicons with different conical angles. Opt Express 2017;25(16):19052.
[29] Gurbatov S, Vitrik O, Kulchin Y, Kuchmizhak A. Mapping the refractive index with single plasmonic nanoantenna. Sci Rep 2018;8:3864.
[30] Filipkowski A, Piechal B, Pysz D, Stepien R, Waddie A, Taghizadeh MR, Buczynski R. Nanostructured gradient index microaxicons made by a modified stack and draw method. Opt Lett 2015;40(22):5200–3.
[31] Musigmann M, Jahns J, Bock M, Grunwald R. Refractive-diffractive dispersion compensation for optical vortex beams with ultrashort pulse durations. Appl Opt 2014;53(31):7304–11.
[32] Žukauskas A, Malinauskas M, Brasselet E. Monolithic generators of pseudo-nondiffracting optical vortex beams at the microscale. Appl Phys Lett 2013;103(18):181122.
[33] Sanchez-Padilla B, Žukauskas A, Aleksanyan A, Balčytis A, Malinauskas M, Juodkazis S, Brasselet E. Wrinkled axicons: shaping light from cusps. Opt Express 2016;24(21):24075–82.
[34] Ambrosio A, Marrucci L, Borbone F, Roviello A, Maddalena P. Light-induced spiral mass transport in azo-polymer films under vortex-beam illumination. Nat Commun 2012(3):989.
[35] Syubaev S, Zhizhchenko A, Kuchmizhak A, Porfirev A, Pustovalov E, Vitrik O, Kulchin Y, Khonina S, Kudryashov S. Direct laser printing of chiral plasmonic nanojets by vortex beams. Opt Express 2017;25(9):10214–23.
[36] Omatsu T, Miyamoto K, Toyoda K, Morita R, Arita Y, Dholakia K. A new twist for materials science: the formation of chiral structures using the angular momentum of light. Adv Opt Mater 2019;7(14):1801672.
[37] Moreno E; 2022. Supplementary material: https://github.com/maxwellfree/Paper-Optics-and-Lasers-in-Engineering/blob/main/Supplementary.pdf, Tech. Rep., CTU in Prague.
[38] Lipkin DM. Existence of a new conservation law in electromagnetic theory. J Math Phys 1964;5(5):696–700.
[39] Liu K-S, Tian D-L, Jiang L. Chapter 24 - frontier of inorganic synthesis and preparative chemistry (i) biomimetic synthesis. In: Xu R, Xu Y, editors. Modern inorganic synthetic chemistry. second ed. Amsterdam: Elsevier; 2017. p. 687–721. ISBN 978-0-444-63591-4
[40] Mun J, Kim M, Yang Y, Badloe T, Ni J, Chen Y, Qiu C-W, Rho J. Electromagnetic chirality: from fundamentals to nontraditional chiroptical phenomena. Light Sci Appl 2020;9(139).
[41] Moreno E, Nguyen HD, Stoian R, Colombier J-P. Full explicit numerical modeling in time-domain for nonlinear electromagnetics simulations in ultrafast laser nanostructuring. Appl Sci 2021;11(16):7429.
[42] Moreno E, Fernndez Pantoja MF, Garcia SG, Bretones AR, Gmez Martin RG. Time-domain numerical modeling of THz photoconductive antennas. IEEE Trans Terahertz Sci Technol 2014;4(4):490–500.
[43] Capoğlu IR, Taflove A, Backman V. Angora: a free software package for finite-difference time-domain electromagnetic simulation. IEEE Antennas Propag Mag 2013;55(4):80–93. https://github.com/drjrkuhn/angora
[44] de Granda U. Ugrfdtd: https://www.sembahome.org/semba/ugrfdtd_info/.
[45] Moreno E, Hemmat Z, Roldán JB, Pantoja MF, Bretones AR, García SG. Time-domain numerical modeling of terahertz receivers based on photoconductive antennas. J Opt Soc Am B 2015;32(10):2034–41.
[46] Moreno E, Hemmat Z, Roldn JB, Pantoja MF, Bretones AR, Garca SG, et al. Implementation of open boundary problems in photo-conductive antennas by using convolutional perfectly matched layers. IEEE Trans Antennas Propag 2016;64(11):4919–22.
[47] Moreno E, Cruz-Hernndez P, Hemmat Z, Mojab A, Michael E. Comparative study of grids based on the cubic crystal system for the FDTD solution of the wave equation. Math Comput Simul 2019;166:395–409.
[48] Sohrabi R, Moreno E, Michael EA. Total field scattering field formulation in a non-uniform grid by means of FDTD-DPW. Electromagnetics 2020;40(1):40–55.
[49] Moreno E, Gonzlez P, Emadi R, Roldn J, Michael E. BCC-Grid versus SC-Grid in the modeling of a sheet of graphene as a surface boundary condition in the context of ADE-FDTD. Math Comput Simul 2021;186:52–61. MATCOM Special Issue MACMAS 2019: First International Conference on Mathematical and Computational Modelling, Approximation and Simulation
[50] Videos: https://www.youtube.com/watch?v=tntf86ou7-o&list=PLP8OUpju_kws2MqXEZM_jXnHaaiYM90WB.